Where the Score Lives: A Wavelet View of Diffusion

Anonymous Author
Anonymous Institution

Abstract

Score-based generative models have had remarkable success over the last decade in generating a diverse set of visually plausible images. A variety of architectures including CNNs, U-Nets, and Transformers have been used as the score-approximation network in such diffusion modeling; however, to date, relatively little is known about how these architectural choices impact generative behavior. In this work, to provide insight into this area, we propose an analytically solvable parameterization of the score function using an expansion in a 2D orthogonal wavelet basis. In particular, we derive interpretable optimal score functions in terms of the moments of the data distribution. We use this parametrization to provide an architecture-agnostic, moment-based analysis that reveals which attributes of the data distribution tend to matter most for denoising. Our score machine is flexible enough to partially mimic the relevant inductive biases of multiple architectures, including U-Nets, and CNNs, taking a step towards understanding why different score architectures can exhibit distinct generative behavior. Since our score is solvable in terms of the moments of the data, we can begin to understand how the data distribution interacts with the score network to produce the behavior we observe in diffusion models.

1 Introduction

Diffusion models have rapidly advanced image generation and many other generative tasks in recent years (Sohl-Dickstein et al., 2015; Song and Ermon, 2019; Ho et al., 2020; Karras et al., 2022; Lou et al., 2024). However, it is still not clear what causes their remarkable ability to construct visually coherent samples which often generalize beyond their training distribution. This generalization property clearly depends both on the score network used and on the underlying properties of the data distribution; since it is clear that a diffusion model trained on a single image would not generalize well.

Recent work has explored both architectural contributions to the kind of creativity displayed in diffusion (Kamb and Ganguli, 2024) and data-determined contributions (Wang and Vastola, 2024). On the architectural side Kamb and Ganguli (2024) demonstrate that a CNN encodes certain inductive biases (namely translation equivariance) into a denoising network when used as a diffusion backbone, encouraging a certain 'patch mosaic' form of creativity; building on prior work Li et al. (2024) which demonstrates that under certain conditions, the ideal score simply memorizes the training data.

On the data-distribution side, spatial locality has been shown to dominate denoising across time scales (Niedoba et al., 2025), and a first-order Gaussian score has additionally been shown to explain a significant amount of observed behavior (Wang and Vastola, 2024). Generalization grows with dataset size (Bonnaire et al., 2025), and learned scores can be interpreted as shrinkage in a geometry-adapted harmonic basis (Kadkhodaie et al., 2024). Yet, it still remains unclear which distributional statistics, and which score network architectural choices, are most critical to score learning – questions central to understanding and improving diffusion models.

In this work, we propose an interpretable parameterization of the score function using an expansion in a wavelet basis, which is remarkably flexible. We then derive an ideal score function particular to our functional form, and implement a wavelet-based score machine. Empirically, we run extensive experiments across different families of denoisers to understand which components of the data distribution are most relevant in which settings.

1.1 Diffusion Background

We first provide a short overview of score-based generative modeling. Diffusion models operate by corrupting all of the input data over time according to a noising process, given by an Ornstein-Uhlenbeck stochastic

Preliminary work. Under review by AISTATS 2026. Do not distribute.

differential equation (Song et al., 2021):

$$d\mathbf{X}_t = \underbrace{f(\mathbf{X}_t, t)}_{\text{drift}}\, dt + \underbrace{g(t)}_{\text{diffusion}}\, dW. \tag{1}$$

The reverse process is given by:

$$d\mathbf{X}_t = \left[f(\mathbf{X}_t, t) - \frac{1}{2} g(t)^2 \underbrace{\nabla_{X_t} \log(p_t(X_t))}_{\text{score function}} \right] dt + g(t) d\bar{W}. \tag{2}$$

We parametrize a neural network s_θ to approximate the score function, and in our setup, we use the score matching objective (Hyvärinen, 2005):

$$\mathcal{L}(\theta) = \int_0^T \lambda(t) \mathbb{E}_{p_t(\mathbf{X})}[||s(\mathbf{X}, t) - s_\theta(\mathbf{X}, t)||_2^2] \tag{3}$$

Where λ is a time dependent weight. For simplicity, in our case, we set $\lambda(t) \equiv 1$. To further simplify, we'll divide our time interval $[0, 1]$ into N discrete steps, and treat each step independently, so the loss decouples across time. Our loss at any particular timestep is

$$\mathcal{L}^{(t)}(\theta) = \mathbb{E}_{p_t(\mathbf{X})}[||s(\mathbf{X}, t) - s_\theta(\mathbf{X}, t)||_2^2] \tag{4}$$

and our overall loss is simply the sum of all such $\mathcal{L}^{(t)}$. In the following, we will demonstrate how to parametrize the score function instead in a wavelet basis, and thereby find the optimal parameters exactly in closed form.

1.2 Wavelets and Denoising

Wavelets have long been used for image denoising and representation. Mallat (1989) introduced multiresolution analysis (MRA) and a fast algorithm for the discrete wavelet transform. Classical wavelet denoising by soft thresholding was developed by Donoho and Johnstone (1994), and further in (Donoho, 1995; Daubechies, 1992; Chang et al., 2000; Portilla et al., 2003), with related analytic multiscale constructions such as wavelet scattering networks (Bruna and Mallat, 2013) and the steerable pyramid (Simoncelli and Freeman, 1995). More recently, Phung et al. (2023) have attempted to use wavelets to speed up diffusion sampling and other score-based generative frameworks, as in (Guth et al., 2022). Like Fourier methods, wavelet decompositions represent square-integrable functions in a basis indexed by "frequencies," but unlike Fourier bases, wavelets are localized in both space and scale, providing joint spatial–frequency resolution. Empirically, it has been found that many U-Nets implement wavelet-like multiresolution computations with Haar-like filters (Falck et al., 2023), motivating our usage of them to approximate the score functions typically learned by U-Nets.

We adopt compactly supported Daubechies wavelets (Fig. 1). Let ϕ denote the scaling ("father") function and ψ the wavelet ("mother") function in one dimension.

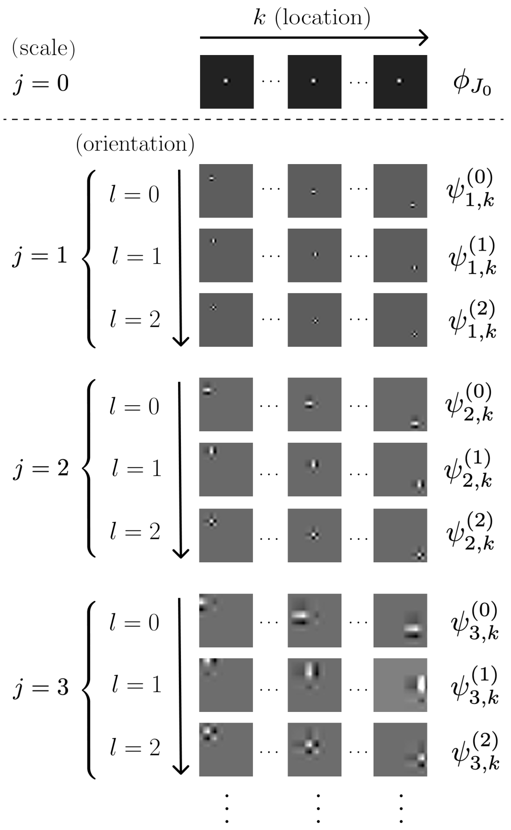

Figure 1: **Daubechies Wavelets.** Visualized across scales j, locations k, and orientations l. We see that at the coarsest scale J_0, only the scale atom is kept, while orientations are included for finer detail wavelets.

In two dimensions we form tensor products to obtain one scaling atom and three detail atoms at each location/scale. The translates and dilates of these functions form an orthogonal basis of the entirety of $L^2(\mathbb{R}^2)$.

For scale $j \in \mathbb{Z}$ and translation $k = (k_1, k_2) \in \mathbb{Z}^2$:

$$\begin{aligned} \phi_{j,k}(\mathbf{u}) &= 2^j\, \phi(2^j u_1 - k_1)\, \phi(2^j u_2 - k_2), \\ \psi^{(\ell)}_{j,k}(\mathbf{u}) &= 2^j\, g^{(\ell)}(2^j u_1 - k_1,\, 2^j u_2 - k_2), \qquad \ell \in \{0, 1, 2\}, \end{aligned}$$

where $g^{(0)}(a, b) = \psi(a)\phi(b)$, $g^{(1)}(a, b) = \phi(a)\psi(b)$, and $g^{(2)}(a, b) = \psi(a)\psi(b)$. While the functions ϕ and ψ are not available in closed form for the Daubechies wavelets, for integer $N \geq 1$, the Daubechies–N wavelet $\psi(x)$ and scaling function $\phi(x)$ are defined by the two-scale relations:

$$\begin{aligned} \phi(x) &= \sqrt{2} \sum_{n=0}^{2N-1} h_n\, \phi(2x - n), \\ \psi(x) &= \sqrt{2} \sum_{n=0}^{2N-1} g_n\, \phi(2x - n). \end{aligned}$$

With periodic boundary handling on $[0, 1]^2$ (our default), the set

$$\mathcal{B}_{J_0} \;=\; \left\{\phi_{J_0,k}\right\}_k \;\cup\; \left\{\psi_{j,k}^{(\ell)}\right\}_{j\geq J_0,\,k,\,\ell}$$

forms an orthonormal basis of $L^2([0,1]^2)$. (Here J_0 is the coarsest scale; only the scaling atoms at J_0 are kept, while all finer detail wavelets $\psi_{j,k}^{(\ell)}$ are included for $j \geq J_0$.) At each fixed (j,k), the triple $\left(\psi_{j,k}^{(1)}, \psi_{j,k}^{(2)}, \psi_{j,k}^{(3)}\right)$ are the three orientation components often called the "horizontal", "vertical", and "diagonal" details. We refer to this per-location orientation triplet as the detail band at (j,k).

1.3 Our Contributions

Concretely, this work offers four core contributions:

- **Analytic wavelet score.** We parameterize the score in an orthonormal wavelet basis and, via Stein's identity, reduce each coefficient to a closed-form ridge least-squares estimate with moment-based right-hand sides.
- **Structured dependencies.** We introduce three interpretable classes which serve to isolate the statistics that matter across noise scales.
- **Empirical findings.** On MNIST (32×32 & 64×64) we find: higher polynomial degree lowers MSE; *local* coupling is most reliable across σ; *band-tying* sharpens edges but can raise MSE at low signal-to-noise ratio; benefits of wavelets increase with resolution.
- **Against trained baselines.** Compared to CNN/U-Net denoisers, our models narrow the gap at low–moderate noise by explicitly encoding short-range, multiscale locality—without gradient-based training and with interpretable coefficients.

2 A Wavelet Expansion of the Score

2.1 Expanding the Score

Let $\langle f,g\rangle = \int_{[0,1]^2} f(\mathbf{u})\,g(\mathbf{u})\,d\mathbf{u}$ denote the L^2 inner product. For a grayscale image X_t at noise level t and score $s_{\text{true}}(\cdot,t)$, since wavelets form an orthonormal basis of L^2, the score at time t in a grayscale image can be expanded as

$$s^{(t)}(X_t) \;=\; \sum_{i\in\mathcal{I}} c_i(X_t)\,w_i, \quad c_i(X_t) = \langle s_{\text{true}}(X_t,t),\, w_i\rangle, \tag{5}$$

where $\{w_i\}_{i\in\mathcal{I}} = \mathcal{B}_{J_0}$ indexes (J_0,k) for scaling atoms and (j,k,ℓ) for detail atoms (visualized in Figure 2). The way in which we choose to model $\langle s_{\text{true}}(X_t), w_i\rangle$ determines the properties of the score function estimator.

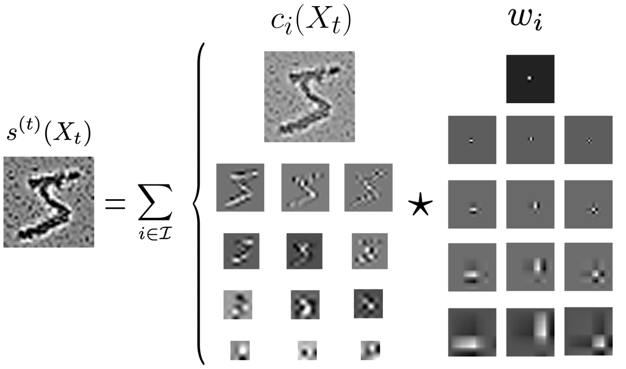

Figure 2: **Wavelet Expansion of the Score**. The score of a given image X_t can be expanded in an orthonormal wavelet basis by representing it as a sum of coefficients $c_i(X_t)$ multiplied by corresponding wavelets w_i (Equation 5). Since the wavelets come in many translated copies, we only display wavelets at a single spatial location k, and display coefficients in spatially ordered 'feature maps'. The sum over spatial locations is then implied by the convolution operator ($\star$).

We model each coefficient by features $\varphi_i(X_t) \in \mathbb{R}^{d_i}$ and parameters $\alpha_i^{(t)} \in \mathbb{R}^{d_i}$ (visualized in Fig. 3):

$$\widehat{c}_i(X_t) \;=\; \alpha_i^{(t)\top}\varphi_i(X_t), \quad s_\theta^{(t)}(X_t) \;=\; \sum_{i\in\mathcal{I}} \widehat{c}_i(X_t)\,w_i. \tag{6}$$

Because $\{w_i\}$ is orthonormal, the population squared loss decouples across i and so taking the gradient w.r.t. $\alpha_i^{(t)}$ yields the simultaneous equations

$$\mathcal{L}^{(t)}(\theta) = \mathbb{E}_{X_t\sim p_t}\left\|s(X_t) - \sum_i \alpha_i^{(t)\top}\varphi_i(X_t)w_i\right\|_{L^2}^2 \tag{7}$$

$$\Rightarrow \frac{\partial\mathcal{L}^{(t)}}{\partial\alpha_i^{(t)}} = -2\mathbb{E}\Big[\varphi_i(X_t)\big(\langle s(X_t),w_i\rangle - \alpha_i^{(t)\top}\varphi_i(X_t)\big)\Big] = 0 \tag{8}$$

Solving for the optimal coefficients $\alpha_i^{(t)*}$, we find, if $\Sigma_i = \mathbb{E}[\varphi_i\varphi_i^\top]$ is invertible:

$$\underbrace{\mathbb{E}[\varphi_i\varphi_i^\top]}_{\Sigma_i}\,\alpha_i^{(t)} = \mathbb{E}\big[\varphi_i(X_t)\,\langle s(X_t),w_i\rangle\big] \tag{9}$$

$$\Rightarrow \quad \alpha_i^{(t)\star} = \Sigma_i^{-1}\,\mathbb{E}\big[\varphi_i(X_t)\,\langle s(X_t),w_i\rangle\big] \tag{10}$$

We can further simplify, by applying a more general form of Stein's Identity as in (Hyvärinen, 2005) to the expectation of the inner product. In particular, for some function f, Stein's Score Identity says

$$\mathbb{E}_{X\sim p_t}\big[\,s_t(X)\cdot f(X)\,\big] \;=\; -\,\mathbb{E}_{X\sim p_t}\big[\nabla\cdot f(X)\,\big] \tag{11}$$

for p_t smooth and under vanishing boundary flux (e.g., periodic boundaries). In our case, we write $\varphi_i(X_t) = [\varphi_{i,1}(X_t),\ldots,\varphi_{i,d_i}(X_t)]^\top$. For each component j, apply Stein's identity with the vector field

$$f_j(x) \;=\; \varphi_{i,j}(x)\,w_i, \qquad \|w_i\|_2 = 1.$$

Then

$$\begin{aligned} \mathbb{E}\big[\varphi_{i,j}(X_t)\,\langle s_t(X_t), w_i\rangle\big] &= -\,\mathbb{E}\big[\nabla_{X_t}\big(\varphi_{i,j}(X_t)\,w_i\big)\big] && (12)\\ &= -\,\mathbb{E}\big[\langle \nabla_{X_t}\varphi_{i,j}(X_t),\, w_i\rangle\big] && (13) \end{aligned}$$

Stacking over $j = 1, \ldots, d_i$ gives the vector form

$$\mathbb{E}\big[\varphi_i(X_t)\,\langle s_t(X_t), w_i\rangle\big] \;=\; -\,\mathbb{E}\big[(\nabla\varphi_i(X_t))^\top w_i\big] \quad (14)$$

Thus, we find that our solution is

$$\alpha_i^{(t)\star} \;=\; -\mathbb{E}[\varphi_i\varphi_i^\top]^{-1}\;\mathbb{E}\big[(\nabla\varphi_i(X_t))^\top w_i\big] \quad (15)$$

In practice, expectations are replaced by sample averages over n training images at time t, $\mathbb{E}[f(X_t)] \approx \frac{1}{n}\sum_{r=1}^{n} f\big(X_t^{(r)}\big)$. We also add a ridge regularization term, because $\hat{\Sigma}_i$ can be singular or ill-conditioned with high-degree features or correlated wavelet coefficients, we stabilize and control variance by adding a ridge regularization, as follows

$$\hat{\alpha}_i^{(t)} \;=\; \big(\hat{\Sigma}_i + \gamma I\big)^{-1}\hat{b}_i, \quad \gamma > 0,$$

which guarantees an invertible system and mitigates overfitting.

Thus, for samples $\{X_t^{(n)}\}_{n=1}^{N}$ and ridge $\gamma \geq 0$,

$$\hat{\alpha}_i^{(t)}(\gamma) = \left(\frac{1}{N}\sum_{n=1}^{N}\varphi_i^{(n)}\varphi_i^{(n)\top} + \gamma I\right)^{-1} \cdot \left(-\frac{1}{N}\sum_{n=1}^{N}(\nabla\varphi_i(X_t^{(n)}))^\top w_i\right). \quad (16)$$

We estimate $\nabla\varphi_i(X_t^{(n)})$ analytically from the chosen features using the method of moments.

Diagonalizing $\Sigma_i = U\Lambda U^\top$ shows that $(\Sigma_i + \gamma I)^{-1}$ weights eigen-directions by $1/(\lambda+\gamma)$. Thus, given that the features are well suited to the data such that Σ_i in (9) is well conditioned and its columns are not highly correlated, the estimator weights eigen directions by $\frac{1}{\lambda+\gamma}$. Small-λ directions receive higher coefficients but are more noise sensitive, which the ridge regression helps to limit. Intuitively, what this says is that this score approximator emphasizes lower-variance feature directions (small λ) and down weights higher-variance directions (large λ). This aligns with the observation that natural images exhibit approximately power-law spectral decay and sparse wavelet coefficients, whereas white noise spreads energy more uniformly; consequently, informative structure often concentrates in a subset of scales and orientations. The model learns to correct more strongly along low-variance modes of the data distribution and ignore the high-variance ones.

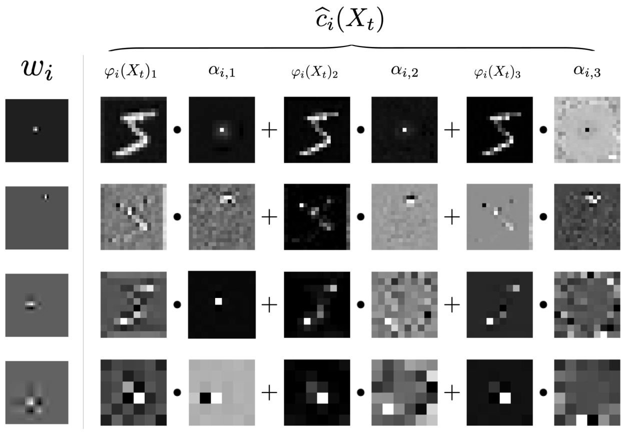

Figure 3: **Wavelet Coefficient Approximation**. We approximate the unknown true coefficients $c_i(X_t)$ of the true score function as an inner product of features $\varphi_i(X_t)$ and parameters $\alpha_i^{(t)}$. The features depicted here are *independent* degree 3 polynomial features.

2.2 Correlation Structures in the Data

Natural images exhibit structured dependencies in the wavelet domain: heavy–tailed marginals per coefficient, co-activation across orientations at a fixed location, and spatial persistence along edges and textures (Wainwright and Simoncelli, 1999). As the noise level decreases, these dependencies become more pronounced. We therefore study three families that isolate, then incrementally reintroduce, these correlations.

(i) *Independent (diagonal).* We model each coefficient $y_t^{(i)} = \langle X_t, w_i\rangle$ in isolation using degree–D monomials (or probabilists' Hermite polynomials for numerical stability). This "mean-field" score approximator is the right baseline when p_t is close to a product distribution (early time steps, near-Gaussian), and it makes failures highly interpretable: any gap to stronger models directly measures the predictive value of cross-coefficient structure that a diagonal model cannot use.

(ii) *Band-tied.* At a fixed scale and location (j, k), we couple the three detail orientations $\ell \in \{0, 1, 2\}$ with degree–D interactions (each monomial includes the target coordinate). This targets cross-orientation co-activation caused by edges and corners and mirrors the channel-mixing inductive bias of CNN/U-Net score networks at a single spatial site. Improvements here isolate the contribution of within-pixel, within-scale structure—testing whether local orientation interactions alone explain denoising gains as t decreases.

(iii) *Local-coupled.* At fixed scale and orientation, we allow the coefficient at location k to depend on neighbors $k+\delta$ within a Chebyshev ball $\|\delta\|_\infty \leq r$. This realizes a small neighborhood in wavelet space and emulates the increasing receptive field of convolutional (or locally attentive) score networks. Gains that grow then saturate with r quantify how much spatial context the score actually needs for accurate denoising and globally consistent structure as noise recedes.

We use (14) to build families of models that probe how scale/orientation structure in the data influences the score. We propose three families of models which can provide insight into what properties of the data distribution are relevant for score-based diffusion. In the Daubechies wavelet setting, we have

$$s_\theta(X_t)^{(t)}(\mathbf{u}) = \sum_{k=(0,0)}^{(2^{J_0}-1,2^{J_0}-1)} \theta_k(X_t,t)\,\phi_{J_0,k}(\mathbf{u}) + \sum_{j=J_0}^{J_{\max}} \sum_{k=(0,0)}^{(2^j-1,2^j-1)} \sum_{l=1}^{3} \zeta_{j,k,l}(X_t,t)\,\psi_{j,k}^{(l)}(\mathbf{u}) \tag{17}$$

where J_0 is the coarsest scale of the approximation, analogous to the spatial resolution at the network's bottleneck and for an image of dimension $H \times W$ $J_{\max} = \lfloor \log_2(\min(H,W)) \rfloor$, which corresponds to the highest level of wavelet detail encoded.

2.2.1 Independent Baseline

Assume (unrealistically) that coefficients decouple across scale j, location k, and detail band l. Let $y_t^{(i)} = \langle X_t, w_i\rangle$ with moments $\mu_r^{(i)}(t) = \mathbb{E}\big[(y_t^{(i)})^r\big]$ and model our coefficients as

$$\theta_k(X_t,t) = \sum_{m=0}^{D} b_m^{(k)}(t)\,\langle X_t, \phi_{J_0,k}\rangle^m, \tag{18}$$

$$\zeta_{j,k,\ell}(X_t,t) = \sum_{m=0}^{D} d_m^{(j,k,\ell)}(t)\,\langle X_t, \psi_{j,k}^{(\ell)}\rangle^m. \tag{19}$$

Using (14) with monomial features gives the normal equations analogous to (7)for each index i and $r = 0,\dots,D$,

$$\sum_{m=0}^{D} a_m^{(i)}(t)\,\mu_{m+r}^{(i)}(t) \;=\; -\,r\,\mu_{r-1}^{(i)}(t),\;\; a_\bullet^{(i)} \in \{b_\bullet^{(k)},\, d_\bullet^{(j,k,\ell)}\},$$

This is a Hankel system $H^{(i)}(t)\,a^{(i)}(t) \;=\; -\,h^{(i)}(t)$, where

$$H_{r,m}^{(i)}(t) = \mu_{r+m}^{(i)}(t),$$
$$h^{(i)}(t) = \big[\,0,\; \mu_0^{(i)}(t),\; 2\mu_1^{(i)}(t), \dots, D\mu_{D-1}^{(i)}(t)\,\big]^\top.$$

Observe that all entries of $H^{(j,k,l)}(t)$ and $h^{(j,k,l)}(t)$ are computable from clean-data raw moments of $Y_0 = \langle X_0, \psi_{j,k}^{(l)}\rangle$.

$$\mu_r^{(i)}(t) = \sum_{m=0}^{r} \binom{r}{m}\,\bar{\alpha}_t^{\frac{m}{2}}\,(1-\bar{\alpha}_t)^{\frac{r-m}{2}}\,\mathbb{E}\big[\langle X_0, w_i\rangle^m\big]\mathbb{E}[Z^{r-m}]. \tag{20}$$

For small D, we can easily compute $a^{(i)}(t) = -(H^{(i)}(t))^{-1}h^{(i)}(t)$ (or $(H^{(i)} + \gamma I)^{-1}$ with ridge $\gamma \geq 0$). The co-factor formula for the coefficients reads

$$\hat{\alpha}_i(t) \;=\; -\,\frac{1}{\det H^{(i)}(t)} \sum_{r=1}^{D} r\,\mu_{r-1}^{(i)}(t)\;C_{r,m}^{(i)}(t) \tag{21}$$

with $C_{r,m}^{(j,k,\ell)}(t)$ the (r,m)-cofactor of $H^{(i)}(t)$. This closed form can be used to investigate how higher order moments of the data distribution impact the score. Though clearly independence is an unrealistic assumption, this model is fast and interpretable, and serves as (i) an initial baseline, and (ii) a diagnostic lower bound. We can investigate the value of different kinds of correlation by measuring the difference in performance between models with different kinds of limited dependence. Allowing each coefficient to depend arbitrarily on *all* wavelet coordinates $y_t = (\langle X_t, w_1\rangle, \dots, \langle X_t, w_n\rangle)$—i.e., learning n functions $f_i : \mathbb{R}^n \to \mathbb{R}$ or even degree–D multivariate polynomials—leads to combinatorial parameter growth and brittle estimation. We therefore restrict to *structured*, computationally tractable, and interpretable dependencies (diagonal/independent, band-tied, and local-coupled), which retain closed-form or efficient normal-equation solvers while capturing the dominant correlations.

2.2.2 Wavelet Band Coupling

One very natural form of correlation is to allow wavelet coefficients at the same scale j and location k to depend on one another. Let $y_0 = \langle X_t, \psi_{j,k}^{(0)}\rangle$, $y_1 = \langle X_t, \psi_{j,k}^{(1)}\rangle$, $y_2 = \langle X_t, \psi_{j,k}^{(2)}\rangle$, At each scale/location in the detail bands (j,k,l), we assume a polynomial coefficient form of degree D:

$$\begin{aligned}
\zeta_{j,k,0}^{(t)}(X_t) &= C_0^{(t)} + \sum_{a=1}^{D}\sum_{b=0}^{D-a}\sum_{c=0}^{D-a-b} \beta_{a,b,c}^{(0)}\,y_0^a y_1^b y_2^c,\\
\zeta_{j,k,1}^{(t)}(X_t) &= C_1^{(t)} + \sum_{b=1}^{D}\sum_{a=0}^{D-b}\sum_{c=0}^{D-b-a} \beta_{a,b,c}^{(1)}\,y_0^a y_1^b y_2^c, \qquad (22)\\
\zeta_{j,k,2}^{(t)}(X_t) &= C_2^{(t)} + \sum_{c=1}^{D}\sum_{a=0}^{D-c}\sum_{b=0}^{D-c-a} \beta_{a,b,c}^{(2)}\,y_0^a y_1^b y_2^c.
\end{aligned}$$

The constraint ensures each monomial contains the target coordinate y_ℓ at least once; cross terms are allowed but pure "other-orientation" terms are excluded.) We define our θ coefficients as polynomials with the same optimal values as in the independent case. Estimation proceeds via the same normal-equation machinery as in (14), but with mixed moments at (j,k):

$$\mu^{(j,k)}_{pqr}(t) := \mathbb{E}\big[\, y_0^p y_1^q y_2^r \,\big], \qquad p+q+r \le D+1,$$

which, under the forward process with orthonormal $\{\psi^{(\ell)}_{j,k}\}$, expand into clean-data mixed moments and factorized Gaussian noise moments.

2.2.3 Local Coupling

Another natural choice of coupling is to allow wavelets in the same local neighborhood. For a radius $r \in \mathbb{N}$, define the neighborhood $\Delta_r = \{\delta \in \mathbb{Z}^2 : \|\delta\|_\infty \le r,\ \delta \ne (0,0)\}$ We allow wavelets in the same neighborhood to interact. Fixing a scale j and orientation $\ell \in \{0,1,2\}$, let the oriented wavelet/detail coefficient at spatial location $k \in \mathcal{K}$ be $y_k = \langle X_t, \psi^{(\ell)}_{j,k} \rangle$. Let $D \ge 1$ be the total degree. Define $S_D = \{(d,e) \in \mathbb{N}^2 : d,e \ge 1,\ d+e \le D\}$. We define the functional forms of θ as follows:

$$\theta_{J_0,k}(X_t,t) = \sum_{i=0}^{D} \alpha_i \left\langle X_t,\ \phi_{J_0,k} \right\rangle^{i} + \sum_{\delta\in\Delta_r} \sum_{(d,e)\in S_D} \beta_{\delta,d,e} \left\langle X_t,\ \phi_{J_0,k} \right\rangle^{d} \left\langle X_t,\ \phi_{J_0,k+\delta} \right\rangle^{e}$$

where α_i and $\beta_{\delta,d,e}$ are the parameters over which we optimize. Similarly for ζ we define

$$\zeta_{j,k,l}(X_t,t) = \sum_{i=0}^{D} \xi_i \left\langle X_t, \psi_{j,k,l} \right\rangle^{i} + \sum_{\delta\in\Delta_r} \sum_{(d,e)\in S_D} \omega_{\delta,d,e} \left\langle X_t, \psi_{j,k,l} \right\rangle^{d} \left\langle X_t, \psi_{j,k+\delta,l} \right\rangle^{e}$$

where ξ_i and $\omega_{\delta,d,e}$ are the parameters over which we optimize. As in the wavelet band coupling, estimation proceeds via the same machinery as in (14), but with mixed moments.

3 Methods

In order to implement this we return to the most general framing of the problem: ridge-regression in a non-linear feature space defined by wavelet coefficients.

Preprocessing We begin by preprocessing the images by normalizing them to $[0,1]$ and resizing them. We use compactly supported Daubechies (db2) wavelets with periodized boundaries. The 2-D tensor-product basis $\mathcal{B}_{J_0}$ includes scaling atoms at the coarsest kept scale J_0 and detail atoms for $j \ge J_0$ up to $J_{\max} = \lfloor \log_2 \min(H,W) \rfloor$ (here $J_{\max} = 3$ at 32×32 in order to avoid boundary effects) with three orientations $\ell \in \{0,1,2\}$. The resulting basis forms an approximately orthonormal linear operator, $B \in \mathbb{R}^{p\times d}$ where p is the number of features and $d = H \times W$ is the flattened dimension of the image. B maps vectorized images $X_t \in \mathbb{R}^d$ to wavelet coefficients.

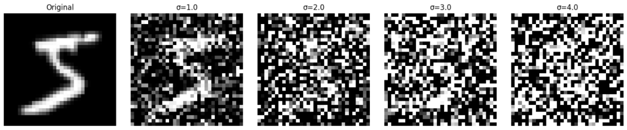

Figure 4: **Visualization of noise regimes.** Clean image $\sigma = 0$ (left) to highly noised $\sigma = 4$ (right)

Noise Model We add Gaussian noise according to the variance exploding regime $X_t = X_0 + \sigma Z$ for $Z \sim \mathcal{N}(0,1)$. We consider four noise regimes in the below experiments, $\sigma \in \{1,2,3,4\}$ (see Fig. 4). This yields noise projections $c = X_t B^T$ that serve as inputs to our non-linear feature constructions. In practice, because B is over-complete and therefore not exactly orthonormal, we use a generalized inverse of B instead.

Feature Expansion and Regression We generate the non-linear features according to the model of correlation we're interested in. In practice we solve the ridge regularized optimization

$$\widehat{W}_\gamma \;=\; \arg\min_{W} \frac{1}{N}\|AW - B\|_F^2 + \gamma\|W\|_F^2 \tag{23}$$

Lemma (Informal) The optimal W from this equation yields the same denoised predictions as our wavelet by wavelet approach in Equation 15 up to some small approximation error.

Lemma (Formal) If there exists a left-inverse $R \in \mathbb{R}^{d\times M}$ such that $R^\top B = I_d$, then letting $F : \mathbb{R}^M \to \mathbb{R}^P$ be any fixed feature map and writing $\varphi(x) := F(xB^\top)$, we have that for X_t and X_0 the two ridge problems yield the same optima.

$$\textbf{(Pixel)}\quad W^\star_\gamma \in \arg\min_{W\in\mathbb{R}^{P\times d}} \mathbb{E}\big[\|\varphi(X_t)W - X_0\|^2\big] + \gamma\|W\|_F^2,$$

$$\textbf{(Coeff)}\quad U^\star_\gamma \in \arg\min_{U\in\mathbb{R}^{P\times M}} \mathbb{E}\big[\|F(X_tB^\top)U - X_0B^\top\|^2\big] + \gamma\|U\|_F^2. \tag{24}$$

Then the minimizers satisfy

$$W^\star_\gamma \;=\; U^\star_\gamma R^\top, \text{ and hence } \varphi(x)W^\star_\gamma \;=\; F(xB^\top)U^\star_\gamma R^\top \quad \forall x.$$

In particular, the denoised predictions produced by the pixel-space ridge and by the wavelet-by-wavelet ridge followed by synthesis agree exactly. We defer the proof of this equivalence to Appendix C.

We also add a ridge term to improve numerical stability (Hoerl and Kennard, 1970). We additionally experiment with the probabilists' Hermite polynomials to expand our θ and ζ with increased stability. The probabilists' Hermite polynomials $\{\mathrm{He}_n(x)\}_{n\ge 0}$ are defined by $\mathrm{He}_n(x) = (-1)^n e^{x^2/2} \frac{d^n}{dx^n} e^{-x^2/2}$ and are orthogonal for $Z \sim \mathcal{N}(0,1)$ with $\mathbb{E}[\mathrm{He}_m(Z)\mathrm{He}_n(Z)] = n!\,\delta_{mn}$. Using He_n in place of raw monomials makes feature vectors orthogonal in expectation under near-Gaussian coordinates $y_t^{(i)}$, reducing covariance and bringing $\Sigma_i = \mathbb{E}[\varphi_i\varphi_i^\top]$ closer to diagonal (hence a smaller condition number). In practice, this improves the conditioning of the matrix equations (9) and yields coefficients less sensitive to scaling and polynomial degree, especially when combined with a small ridge penalty. The results for this model are deferred to Appendix A.

Denoising and Comparison with Models We denoise our images according to $\widehat{X_0} = A\widehat{W}$ and clamp the images back to $[0, 1]$ before computing MSE over the entire dataset. We also compare our reconstruction MSE to that of trained diffusion models with U-Net and CNN backbones. We defer the details of training those models to Appendix B.

4 Experiments and Discussion

With these closed-form equations and model families in hand, we now test how much band and local coupling improve over the independent baseline across different noise levels. These models are just a few examples of the correlation structures in the data that can be probed with this approach.

Setup We evaluate all models on two copies of the full MNIST training set of 60,000 images, one set resized to 32×32 and the other resized to 64×64, denoted MNIST-32 and MNIST-64 respectively.

Changing the Degree of the Approximation As shown in Figure 5 and Figure 6, increasing the polynomial degree consistently improves reconstruction error by enhancing the expressivity of the feature space. The gains are especially pronounced for correlated models—most notably in the local coupling case (Figure 5c)—indicating that higher-order moments of the wavelet-projected data are particularly valuable when modeling correlation structure. Strikingly, this effect is amplified at larger image resolutions: comparing Figure 5 with Figure 6 suggests that our wavelet-based reconstruction becomes more robust as image size increases.

Detail Band Correlation As shown in Figure 5 and Figure 6, coupling the three orientations at a location improves visual quality (see Appendix A). Surprisingly, for both 32×32 and 64×64 images, independent features often achieve lower MSE than the band-tied counterpart. Qualitatively, however, edges and corners are sharper under band-tying, consistent with the hypothesis that cross-orientation co-activation carries most of the local predictive signal and is especially sensitive to sharp changes. This detail-band correlation can be viewed as a non-linear cross-channel interaction (e.g., quadratic products within a scale). At high noise levels ($\sigma \geq 3$), the signal to noise ratio of detail coefficients drops, so cross-orientation terms act on products

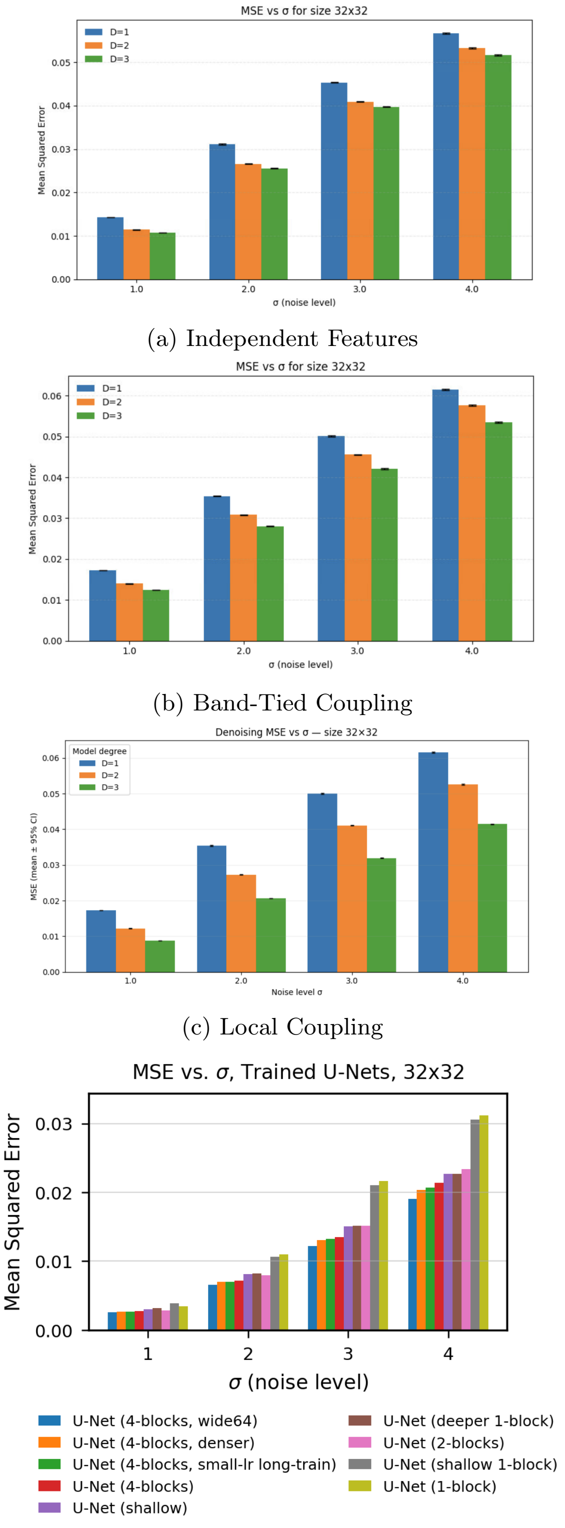

(a) Independent Features

(b) Band-Tied Coupling

(c) Local Coupling

(d) Trained Diffusion Models

Figure 5: **MNIST-32.** **(a)** Denoising MSE with independent monomial features across three sets of features: degrees 1, 2, & 3. **(b)** Same features with band-tied coupling, and **(c)** local coupling. **(d)** Comparable performance of a variety of trained U-Net score function approximators.

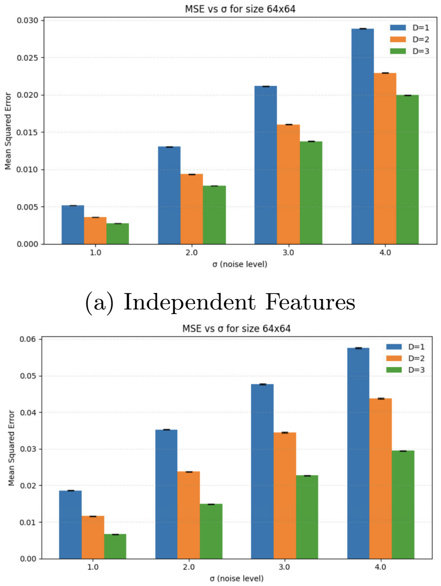

(a) Independent Features

(b) Band-Tied Coupling

Figure 6: **MNIST-64.** Denoising MSE with **(a)** independent features, and **(b)** band-tied coupling on larger images. We see higher degree polynomials are more performant with larger images, compared with Fig. 5.

of noisy coefficients, inflating variance and inducing localized overshoot/undershoot that pixel-space MSE penalizes strongly. In short, channel mixing helps perceptual sharpness but can hurt MSE when the inputs are noise-dominated. This might suggest using noise-aware mixing (e.g., down-weighting cross-orientation features or increasing ridge at large σ), or complementing MSE with structure-sensitive metrics.

Local Correlation Across image sizes (see Figure 5 and Appendix A), we observe that introducing local coupling between neighboring coefficients yields a consistent and significant improvement in denoising MSE. This provides empirical support for prior mechanistic explanations of diffusion models (Niedoba et al., 2025; Kamb and Ganguli, 2024), which emphasize that local interactions are among the most predictive features available to a denoiser. Intuitively, wavelet coefficients corresponding to nearby locations tend to covary strongly, especially along edges, textures, and digit strokes (Wainwright and Simoncelli, 1999; Simoncelli and Olshausen, 2001). By capturing this short-range dependency, the model can recover local structure more effectively than when treating coefficients as independent. Notably, unlike detail-band correlation (which risks performance degradation at high noise due to channel mixing), local correlation maintains benefits across all σ regimes, suggesting that spatial neighborhoods retain informative signal even when individual coefficients are noisy.

Changing Image Size A key advantage of our approach is robustness to increasing image size and resolution. Unlike linear score approximations, the wavelet parameterization preserves locality and multiresolution structure: feature interactions remain confined to small neighborhoods and scales, so the effective design matrices retain near-block-diagonal structure and well-behaved conditioning as $H \times W$ grows. Empirically, the relative performance of our models improves at higher resolutions. Moving from 32×32 to 64×64 yields larger MSE reductions for the same polynomial degree, suggesting that additional scales provide genuinely useful predictive signal rather than simply inflating dimensionality (see Appendix A).

Comparison to Trained Models As introduced by Falck et al. (2023), U-Nets can be viewed as implicitly learning a multiresolution (wavelet-like) representation. In our comparison to trained CNN/U-Net denoisers (Fig. 5d), the learned models outperform our analytic wavelet denoisers across noise levels, as expected. However, two patterns are noteworthy. First, with local coupling and higher polynomial degree, the gap at low to moderate noise ($\sigma \in \{1, 2\}$) narrows noticeably, indicating that much of the benefit of learned models arises from exploiting short-range, multiscale locality, which is the inductive bias encoded in our features. Second, as noise increases ($\sigma \geq 3$), the trained models retain a larger advantage, consistent with their capacity to leverage deeper nonlinearity, cross-scale mixing, and data-dependent priors learned during training. Crucially, our approach achieves these results with no gradient-based training and a single closed-form ridge solve per setting, yielding interpretable coefficients and stable behavior under changes in image size.

5 Conclusion

We introduced an analytically tractable, wavelet–based parameterization of diffusion scores with closed-form normal equations and three structured dependency families (independent, band-tied, local). This framework isolates which attributes of the data distribution contribute to denoising across noise scales and resolutions. Empirically, higher polynomial degree improves accuracy, band-tying sharpens edges but can raise MSE at low SNR, and local coupling yields the most reliable MSE gains across σ and image sizes. The gap to trained CNN/U-Net denoisers narrows at low–moderate noise when locality is encoded explicitly, suggesting that much of their advantage stems from short-range, multiscale interactions that our analytic model captures without gradient-based training. The method is scalable (closed-form per setting), interpretable (moment-level diagnostics), and robust to increasing resolution. Because the score coefficients are solved from moments, the framework serves as a diagnostic tool: it quantifies the value of specific correlations (orientation co-activation vs. spatial neighborhoods), motivates noise-aware channel mixing and ridge schedules, and can inform data-efficient architectural choices and initialization schemes for learned models.

References

Bonnaire, T., Urfin, R., Biroli, G., and Mézard, M. (2025). Why diffusion models don't memorize: The role of implicit dynamical regularization in training.

Bruna, J. and Mallat, S. (2013). Invariant scattering convolution networks. *IEEE Transactions on Pattern Analysis and Machine Intelligence*, 35(8):1872–1886.

Chang, S., Yu, B., and Vetterli, M. (2000). Adaptive wavelet thresholding for image denoising and compression. *IEEE Transactions on Image Processing*, 9(9):1532–1546.

Daubechies, I. (1992). *Ten Lectures on Wavelets.* SIAM.

Donoho, D. (1995). De-noising by soft-thresholding. *IEEE Transactions on Information Theory*, 41(3):613–627.

Donoho, D. L. and Johnstone, I. M. (1994). Ideal spatial adaptation by wavelet shrinkage. *Biometrika*, 81(3):425–455. _eprint: https://academic.oup.com/biomet/article-pdf/81/3/425/26079146/81.3.425.pdf.

Falck, F., Williams, C., Danks, D., Deligiannidis, G., Yau, C., Holmes, C., Doucet, A., and Willetts, M. (2023). A multi-resolution framework for u-nets with applications to hierarchical vaes.

Guth, F., Coste, S., Bortoli, V. D., and Mallat, S. (2022). Wavelet score-based generative modeling.

Ho, J., Jain, A. N., and Abbeel, P. (2020). Denoising diffusion probabilistic models. In *Advances in Neural Information Processing Systems*, volume 33, pages 6840–6851. Curran Associates, Inc.

Hoerl, A. E. and Kennard, R. W. (1970). Ridge regression: Biased estimation for nonorthogonal problems. *Technometrics*, 12(1):55–67.

Hyvärinen, A. (2005). Estimation of non-normalized statistical models by score matching. *Journal of Machine Learning Research*, 6(24):695–709.

Kadkhodaie, Z., Guth, F., Simoncelli, E. P., and Mallat, S. (2024). Generalization in diffusion models arises from geometry-adaptive harmonic representations.

Kamb, M. and Ganguli, S. (2024). An analytic theory of creativity in convolutional diffusion models.

Karras, T., Aittala, M., Aila, T., and Laine, S. (2022). Elucidating the design space of diffusion-based generative models. In *NeurIPS*.

Li, S., Chen, S., and Li, Q. (2024). A good score does not lead to a good generative model.

Lou, A., Meng, C., and Ermon, S. (2024). Discrete diffusion modeling by estimating the ratios of the data distribution.

Mallat, S. (1989). A theory for multiresolution signal decomposition: the wavelet representation. *IEEE Transactions on Pattern Analysis and Machine Intelligence*, 11(7):674–693.

Niedoba, M., Zwartsenberg, B., Murphy, K., and Wood, F. (2025). Towards a mechanistic explanation of diffusion model generalization.

Phung, H., Dao, Q., and Tran, A. (2023). Wavelet diffusion models are fast and scalable image generators.

Portilla, J., Strela, V., Wainwright, M. S., and Simoncelli, E. P. (2003). Image denoising using scale mixtures of gaussians in the wavelet domain. *IEEE Transactions on Image Processing*, 12(11):1338–1351.

Simoncelli, E. P. and Freeman, W. T. (1995). The steerable pyramid: A flexible architecture for multi-scale derivative computation. In *Proc. IEEE Intl. Conf. on Image Processing (ICIP)*, volume 3, pages 444–447.

Simoncelli, E. P. and Olshausen, B. A. (2001). Natural image statistics and neural representation. *Annual review of neuroscience*, 24:1193–216.

Sohl-Dickstein, J., Weiss, E. A., Maheswaranathan, N., and Ganguli, S. (2015). Deep unsupervised learning using nonequilibrium thermodynamics. In *Proceedings of the 32nd International Conference on Machine Learning*, volume 37 of *Proceedings of Machine Learning Research*, pages 2256–2265. PMLR.

Song, J., Meng, C., and Ermon, S. (2020). Denoising diffusion implicit models. *arXiv preprint arXiv:2010.02502*.

Song, Y. and Ermon, S. (2019). Generative modeling by estimating gradients of the data distribution. In *Advances in Neural Information Processing Systems*, volume 32.

Song, Y., Sohl-Dickstein, J., Kingma, D. P., Kumar, A., Ermon, S., and Poole, B. (2021). Score-based generative modeling through stochastic differential equations.

Wainwright, M. J. and Simoncelli, E. (1999). Scale mixtures of gaussians and the statistics of natural images. In Solla, S., Leen, T., and Müller, K., editors, *Advances in Neural Information Processing Systems*, volume 12. MIT Press.

Wang, B. and Vastola, J. J. (2024). The unreasonable effectiveness of gaussian score approximation for diffusion models and its applications.